

# Fully 4D Dynamic Image Reconstruction by Nonlinear Constrained Programming

Stéphan Blinder, *Member, IEEE*, Dominikus Noll, Xavier Hatchondo, Anna Celler, *Member, IEEE*, Jean-Paul, Esquerré *Member, IEEE*, Pierre Payoux and Pierre Gantet

**Abstract**—In standard SPECT with static radio-tracers, the activity distribution in tissue is assumed constant during the acquisition. However, techniques capable of visualizing dynamic tracers may provide new insight into physiology and function of organisms. This is the aim of dynamic SPECT. We developed oSPECT, a new fully 4D reconstruction approach to obtain time activity curves from single or multiple slow rotations with dynamic SPECT data. It is based on KNITRO, a large-scale nonlinear constrained optimization method that takes curvature information into account to speed up convergence. The performance of oSPECT is tested using data from a dynamic anthropomorphic numerical phantom that simulates myocardial perfusion of  $^{99m}\text{Tc}$ -Teboroxime. We also tested the method on a simulated brain study with  $^{123}\text{I}$ -FP-CIT, a dynamic presynaptic marker for SPECT of the dopaminergic neurotransmission system.

**Index Terms**—Dynamic imaging, large scale nonlinear optimization, regularization, simulations, myocardial SPECT, cerebral SPECT

## I. INTRODUCTION

IN STANDARD SPECT with static radio-tracers, the activity distribution in tissue is assumed to remain constant during the acquisition. However, techniques capable of visualizing dynamic tracers may provide new insight into physiology and function of organisms. This is the aim of dynamic SPECT. Dynamic imaging is already a well established technique in Positron Emission Tomography (PET) - at least in a research environment - for brain and cardiac studies e.g. [1-4]. However, PET is an expensive technique of restricted availability. This issue can be overcome with the use of dynamic SPECT, which has proved its potential applicability in clinical studies such as  $\text{Tl-201}$  myocardial imaging [5] and cerebral blood flow measurement [6].

In recent years, several methods to assess tracer dynamics from SPECT studies have been proposed. They can be classified mainly into three groups:

1) A first group includes methods involving data acquired with

fast rotations of the camera. During each rotation, activity distribution is assumed to remain constant and the acquired subset of data is reconstructed with standard SPECT algorithms. The reconstruction of the separate rotations provides a temporal series of spatial activity distributions. The fast acquisition protocol produces a high level of noise and poor image quality. Moreover, multiple rotations generate a very large amount of data to handle and reconstruct. On the other hand, the simplicity of this method and its acceptable accuracy have allowed its clinical application, in particular in myocardium perfusion studies [7, 8].

2) A second group includes methods that assume an a priori kinetic model. In most situation, a one or two compartmental model is used. Some authors have investigated methods to estimate kinetic parameters directly from projections, bypassing the reconstruction step [9-12], whereas others like [13] suggest using a kinetic model in reconstructing explicitly the dynamic activity distribution. However, those methods can only provide results predicted by the input kinetic model and thus may lead in some situations with altered or abnormal physiological functions to incorrect and misleading results.

3) A third approach to the problem is to reconstruct the spatio-temporal activity distribution by direct inversion of the tomographic dynamic problem. Mathematically, such problem is modelled by an underdetermined linear system and involves the inversion of a huge, ill-conditioned matrix. A straightforward inversion had been attempted by [14] using the conventional *Singular Value Decomposition* inversion algorithm in order to calculate a weighted least squares solution according to Poisson statistics. Unfortunately, it took a full week to reconstruct a single slice on a 300MHz CPU. Furthermore, the authors stress the very high level of noise in their solution.

Two approaches, designed to reconstruct data acquired during a standard slow rotation of the SPECT camera, had been proposed in order to circumvent the instability of this problem:

i) the 3D (2D+time) constrained least squares (CLS) method [15, 16] minimizes a quadratic cost function augmented by regularizing terms subject to bound constraints restricting the temporal variations of activity. The minimization of the cost function is based on the first-order bound-constrained optimization code L-BFGS-B.

ii) the dynamic expectation maximization (dEM) algorithm, originally proposed in [17] and implemented in [18, 19], is a dynamic version of the Maximum Likelihood Expectation Maximization algorithm. It is significantly faster than CLS, but not compatible with any of the more sophisticated regu-

Manuscript received November 15, 2003; revised xxxx. This work was supported in part by the France-Canada Research Foundation.

Stéphan Blinder is with the Department of Radiology, University of British Columbia, Vancouver, B.C., Canada (email: blinder@physics.ubc.ca).

Dominikus Noll is with Mathématiques pour l'Industrie et la Physique, CNRS UMR 5640, Université Paul Sabatier, Toulouse, France (email: noll@mip.ups-tlse.fr).

Anna Celler is with the Division of Nuclear Medicine, Vancouver Hospital and Health Sciences Centre, Vancouver, B.C., Canada (email: aceller@physics.ubc.ca).

Xavier Hatchondo, Jean-Paul Esquerré, Pierre Payoux and Pierre Gantet are with the Laboratoire de Biophysique, Université Paul Sabatier, Toulouse, France (email: hatchond@cict.fr, jesquerr@cict.fr, payoux.p@chu-toulouse.fr, gantet@cict.fr).

larization techniques required for the appropriate treatment of ill-posed problems.

With the aim to improve the quality of dynamic SPECT reconstructions, we have developed oSPECT, a 4D (3D+time) SPECT reconstruction algorithm based on the large scale optimization package KNITRO, a solver which is more powerful and versatile than L-BFGS-B used in the CLS method. oSPECT permits the use of regularizing terms. They stabilize the inversion of the tomographic problem, they have an adjustable spatial and temporal smoothing effect, but may also be designed for edge conservation. As well, they can be designed to take into account *a priori* information such as a physiological temporal behavior or a kinetic model. The regularizing terms impose more or less relaxed constraints, but oSPECT permits also to impose hard equality or inequality constraints in the system which is one of its advantages over the CLS method. Thus oSPECT is a very flexible and versatile tool that can be adapted to various physiological problems and has a great potential of improvements through the use of appropriate constraints and regularizing terms.

We present here the first results of this new algorithm obtained with a choice of elementary regularizers and constraints. The performance of oSPECT was tested on two distinct clinically relevant applications. First, a study of the myocardial perfusion with the dynamic tracer  $^{99m}\text{Tc}$ -Teboroxime was performed using our dMCAT phantom model [20], a dynamic version of the anthropomorphic numerical phantom MCAT. Secondly, we tested oSPECT on a numerical brain model of the dopaminergic neurotransmission system with  $^{123}\text{I}$ -FP-CIT, a dynamic presynaptic marker for SPECT.

## II. METHOD

The method we propose is based on large-scale nonlinear constrained optimization. We consider the program

$$(P) \quad \begin{array}{ll} \text{minimize} & f(x) := \frac{1}{2} \|Rx - p\|_w^2 + \alpha \mathcal{R}eg(x) \\ \text{subject to} & \ell_\nu \leq c_\nu(x) \leq u_\nu, \nu = 1, \dots, I \end{array}$$

The unknown spatio-temporal activity distribution is  $x$ , and  $I$  is the number of inequality constraints  $c_\nu(x)$  with bounds  $\ell_\nu$  and  $u_\nu$  being used to bring prior information about  $x$  into the process. The linear operator  $R$  is a forward projector which in our implementation includes both a *central ray* attenuation correction [21], and a 3D detector response compensation (DRC) as described in [22]. The vector  $p$  represents dynamic SPECT projection data. Further elements of  $(P)$  are the regularizers  $\alpha \mathcal{R}eg(x)$  included to improve stability of the otherwise seriously ill-conditioned problem and several of them have been discussed in the literature e.g. [23]. The data mismatch term  $\frac{1}{2} \|Rx - p\|_w^2$  in principle assumes Gaussian distributed measurements  $p$ , but an appropriate weighting may be used to address the more realistic Poisson distribution [23].

In our approach, the 3D reference volume is *a priori* divided into several types of voxels. Only voxels inside the 3D body contour, defined by a segmentation of the attenuation map, contribute to the activity vector, either by a single value  $x_i$  if voxel  $i$  is classified as *static*, or by a total of  $S$  values  $x_{i,k}$ ,  $k = 1, \dots, S$ , if  $i$  is classified as *dynamic* and the total number of time frames  $k$  considered in the study is  $S$ . The

number of time frames can be at most as large as the number of stops  $S$  of the camera system, but the temporal resolution can be reduced in order to decrease the number of unknowns in the system. In this case, two or more consecutive stops are reconstructed as a single time frame over which the activity distribution is assumed to remain static.

The linear inequality constraints  $c_\nu(x) = x_{i,k} - x_{i,k+1}$  in  $(P)$  apply only to the  $n_{\mathcal{D}YN}$  dynamic voxels  $i \in \mathcal{D}YN$  and the number of these constraints is  $I = (S - 1)n_{\mathcal{D}YN}$ . Then  $\ell_\nu \leq c_\nu(x) \leq 0 =: u_\nu$  says that the activity in voxel  $i$ , between the time steps  $k$  and  $k + 1$ , is increasing or constant, but with a rate of at most  $\ell_\nu$ . Similarly,  $\ell_\nu := 0 \leq c_\nu(x) \leq u_\nu$  says that the activity in voxel  $i$  is decreasing or constant between time steps  $k$  and  $k + 1$ , but with rate no greater than  $u_\nu$ . If an approximate position  $k_p(i)$  of the peak activity for the dynamic voxel  $i$  is estimated, we propose to replace these hard constraints by the more flexible

$$\ell_\nu \leq x_{i,k} - x_{i,k+1} \leq -\tau =: u_\nu,$$

for time frames  $k_p(i) - \Delta k \leq k < k_p(i)$  and

$$\ell_\nu := \tau \leq x_{i,k} - x_{i,k+1} \leq u_\nu$$

for time frames  $k_p(i) \leq k \leq k_p(i) + \Delta k$  and some suitably chosen  $\tau > 0$  and  $\Delta k$ . This allows the method to adjust the tentative peak position  $k_p(i)$  automatically within the confidence interval  $[k_p(i) - \Delta k, k_p(i) + \Delta k]$ , so that errors imposed by the prior information may to some extent be corrected or reduced. Prior peak positions may be calculated either by the method proposed in [18], or by fitting “hat functions” [23] or similar functions. This work is currently in progress.

We shall notice that the problem  $(P)$  can be easily adapted to specific physiological cases through the use of appropriate temporal constraints or regularization when an *a priori* kinetic model is available. The implementation of the kinetic model through the constraints  $c_\nu(x)$  defines a hard constraint whereas its implementation through the regularization terms relaxes this constraint.

## III. OPTIMIZER

In order to solve program  $(P)$  we use the optimizer package KNITRO [24], which is based on a Newton trust region method adapted to large scale nonlinear constrained optimization programs. KNITRO includes second order information to speed up convergence of the algorithm, a novel feature for software addressing very large size problems. In our problem, the Hessian matrix of the objective function  $f(x)$  in  $(P)$  is not sparse and even the coefficients of the 3D forward projection operator  $R$  can not be stored. Incorporating curvature information in  $f(x)$  therefore requires the dialogue technique used by KNITRO, which we indicate by the following schematic code:

```
/* dialogue principle */
initialize;
while ( flag != stop ) {
  case( flag == gimme_f )
    my_evalfc( x,&f,&c,my_parameters );
```

```

case( flag == gimme_g )
  my_evalg( x,&g,my_parameters );
case( flag == gimme_H )
  my_evalH( x,&v,lambda,my_parameters );
knitro( &x,f,c,g,v,&flag );
if( my_stopping_test == true )
  flag = stop;
}
display_results;

```

The optimizer is a `f77` function `knitro` which may be included in the user's master code. The variables  $x$ ,  $f$  and  $c$  represent the current vector  $x$ , the objective function value  $f(x)$  and the values of the constraints  $c_\nu(x)$  in  $(P)$ , while  $g$  regroups the first order information  $f'(x)$  and  $c'_\nu(x)$  at  $x$ . The dialogue principle enables the user to implement at his convenience the functions `my_evalfc`, `my_evalg` and `my_evalH` that calculate the objective function and the constraints, their first derivative and second derivative respectively. This is a major advantage over those large scale codes, which provide as part of the optimizer package, predefined functions `their_evalfc`, `their_evalg`, etc. whose imposed structure greatly hinders the application of user's parameters required for the master code. In contrast, the calling function `knitro` only requires the *results* of those functions, leaving their workout to the user, while keeping the current status of the optimization process stored in the variable `flag`.

The function `my_evalH` that calculates the Hessian  $H(x) = f''(x) + \lambda c''(x)$  of the Lagrangian of  $(P)$  is at the core of the trust region strategy as it allows the use of second order information even when  $H(x)$  could not be stored. Indeed, while  $H(x)$  may even be dense, matrix vector products  $H(x) \cdot v$  with test vectors  $v$  may require much less calculation. The solution of a linear system  $H(x) \cdot \Delta x = b$  required to estimate a step  $\Delta x$  may then be obtained by iterative techniques like conjugate gradient or GMRES, which involve a succession of such products. These matrix vector products are obtained by the function `my_evalH` which calculates the product  $H(x) \cdot v$  for the test vector  $v$ , and returns the result to the optimizer as a new vector  $v$ .

Notice that in our application, the constraint functions  $c_\nu(x)$  are linear, so  $c''_\nu(x) = 0$ , and the calculation of the Hessian of the Lagrangian is reduced to the evaluation of  $f''(x) = R^T R x + \alpha \text{Reg}''(x)$ . Typically, the regularizers are local and therefore have sparse Hessians, so the main computational cost is in the product  $R^T R v$ , whose cost is that of one forward and one backward product with the projection operator  $R$ , so roughly the cost of one iteration of a static EM-algorithm. The same complexity appears at the level of the gradient `my_evalg`, as the structure of  $c'_\nu(x)$  is sparse. The efficiency of KNITRO therefore hinges on a speedy resolution of the system  $H(x) \cdot \Delta x = b$  which depends on the condition number  $\text{cond}(H)$ . Unfortunately, when  $\text{cond}(H)$  is large, the current version of KNITRO does not permit the use of a user provided preconditioner, although the dialogue principle would make its management extremely simple.

A last advantage of the dialogue principle is that the user has a very convenient way to apply his or her own stopping

criterion. Optimizers like KNITRO clearly have their own internal stopping tests, which dispense with the process when first order optimality conditions are attained within a pre-specified tolerance, or when changes in  $x$  become negligible. Whenever such a test applies, the optimizer `knitro` will by itself set `flag = stop`. However, large scale problems often require problem specific stopping tests, which are easily implemented as a consequence of the ongoing interaction between the optimizer and the user.

## IV. SIMULATIONS

### A. Myocardium

In order to evaluate the performance of the dynamic reconstruction method, we used the dynamic numerical phantom dMCAT [20], based on the anthropomorphic numerical phantom MCAT. The dMCAT phantom simulated the myocardial perfusion of the dynamic tracer  $^{99m}\text{Tc}$ -Teboroxime in a healthy patient. A transaxial slice of this phantom is shown in Fig. 1. Time activity curves (TACs) also shown in Fig. 1 were computed using an eight compartment model, including myocardium, left and right ventricles, liver, lungs and muscles. Kinetic parameters and normalization of the model were adjusted to obtain TACs that resemble those observed in real patient data. Projection data were simulated starting 90 seconds post-injection with 32 time steps of 20 seconds each. Each projection contained  $64 \times 64$  bins with a size of 6.25 mm. A standard single rotation cardiac protocol on a dual-head camera was used to generate 64 projections ranging over  $180^\circ$  from right anterior oblique to left posterior oblique. Also, we simulated three studies using multiple on a triple-head camera. Each study contained 96 projections over one, two and three full rotations. The total acquisition time remained unchanged. Noise levels corresponding to realistic count rates were modelled. Both attenuation and 2D Gaussian depth-dependent detector response corresponding to a camera equipped with Low Energy High Resolution (LEHR) collimators were included, but scatter was not modelled.

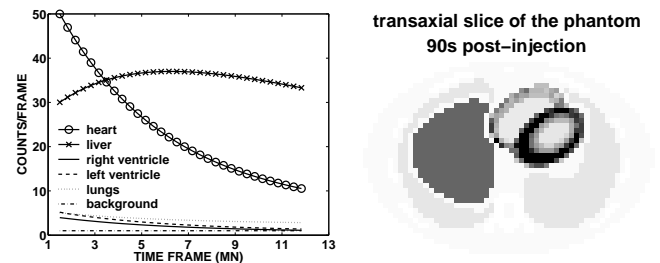


Fig. 1. A transaxial slice of the dMCAT phantom 90 seconds post-injection (right) and the associated time activity curves (left).

### B. Brain

We also tested oSPECT on a numerical model of the dopaminergic neurotransmission system with  $^{123}\text{I}$ -FP-CIT, a dynamic presynaptic marker for SPECT. For this purpose, we created a dynamic numerical brain phantom. The morphology of the phantom shown in Fig. 2 was based on a CT study of a physical brain phantom (RSD - Radiology Support Device).

Then, the striatal region of the phantom was segmented using a threshold method. Five regions were defined: the left and the right putamens and caudate nuclei, as well as a non-specific area representing the surrounding brain region (occipital region). The temporal behavior in each region was determined by solving a five compartment model with kinetic parameters and count rates adjusted in accordance with several  $^{123}\text{I}$ -FP-CIT clinical studies performed at Hôpital Purpan (Toulouse, France) and with some other studies [25, 26]. TACs are also shown in Fig. 2. A cerebral protocol using a triple-head camera was applied to generate 60 projections ranging over  $360^\circ$ . Acquisition started at injection and continued over 20 stops of 1 minute each. Each projection contained  $64 \times 64$  bins with a size of 3.4 mm. Poisson noise, attenuation and 2D Gaussian depth-dependent detector response corresponding to a camera equipped with Low Energy Ultra High Resolution (LEUHR) collimators were taken into account.

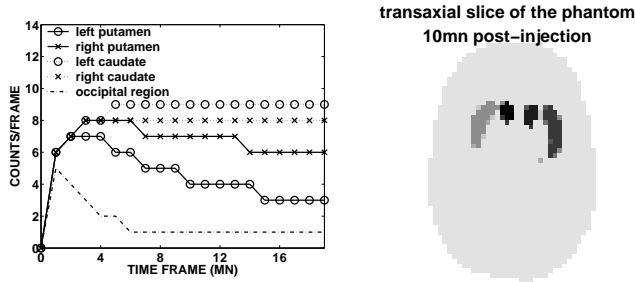


Fig. 2. A transaxial slice of the cerebral phantom 10 minutes post-injection (right) and the associated time activity curves (left).

## V. RECONSTRUCTIONS AND DATA ANALYSIS

Both thorax and brain simulations were reconstructed assuming a Poisson distribution in the projection data and compensating for both attenuation and 1D and 2D Gaussian detector response. Since a regular static reconstruction of dynamic data results in a rough temporal mean of the tracer distribution [20], we used a 3D (static) OSEM solution to create a flat temporal distribution which served as an initial point for the iterative process.

In those reconstructions, the prior information defining the set of constraints  $c_\nu(x)$  in  $(P)$  is summarized in a mask that describes the temporal behavior of the voxels. Four different types of temporal behavior are possible:

- i) TACs constant,
- ii) TACs monotonically increasing,
- iii) TACs monotonically decreasing,
- iv) TACs first increasing and then decreasing.

In this latter case, the temporal position of the peak activity is needed. The methods discussed in [23, 18], in particular the “hat method” may be used to obtain prior estimates of the peak positions. However, in those reconstructions, the temporal mask was not calculated, but directly defined using the true activity distributions.

Since the solution of program  $(P)$  may vary with the choice of regularization, we investigated four spatial and one temporal regularizers  $\text{Reg}(x)$ :

- i) spatial norm-1 symmetric:  

$$\sum_k \sum_{i \in \mathcal{I}N} \sum_{(i_{\text{next}}, i_{\text{prev}})} \sqrt{[x_{i_{\text{next}}, k} - x_{i_{\text{prev}}, k}]^2 + \epsilon}$$

- ii) spatial norm-1 asymmetric:  

$$\sum_k \sum_{i \in \mathcal{I}N} \sum_{i_{\text{prev}}} \sqrt{[x_{i, k} - x_{i_{\text{prev}}, k}]^2 + \epsilon}$$
- iii) spatial Tychonoff symmetric:  

$$\frac{1}{2} \sum_k \sum_{i \in \mathcal{I}N} \sum_{(i_{\text{next}}, i_{\text{prev}})} [x_{i_{\text{next}}, k} - x_{i_{\text{prev}}, k}]^2$$
- iv) spatial Tychonoff asymmetric:  

$$\frac{1}{2} \sum_k \sum_{i \in \mathcal{I}N} \sum_{i_{\text{prev}}} [x_{i, k} - x_{i_{\text{prev}}, k}]^2$$
- v) temporal Tychonoff asymmetric:  

$$\frac{1}{2} \sum_{i \in \mathcal{D}Y\mathcal{N}} \sum_{k=1}^{S-1} [x_{i, k} - x_{i, k+1}]^2$$

With the spatial regularizers, the summation  $\sum_i$  is performed over those pixels  $i \in \mathcal{I}N$  which are located strictly inside the 3D body contour. The pixels  $i_{\text{next}}$  and  $i_{\text{prev}}$  refer to the neighboring pixels of pixel  $i$  along each of the three spatial axes. In order to ensure the differentiability of norm-1 regularizers, a small term  $\epsilon$  was added. With the temporal regularizer,  $\sum_i$  is performed only over dynamic pixels  $i \in \mathcal{D}Y\mathcal{N}$ . The roughness parameter  $\alpha$  of the regularization was adjusted to produce the best compromise between image quality and accuracy of the reconstructed TACs.

In order to analyse and compare reconstructions, we defined two main regions of interest (ROIs) in the thorax phantoms, one over the myocardium and one over the liver, containing 104 and 256 pixels respectively.

On the brain, five ROIs, corresponding to the left and right putamens and caudate nuclei and to the occipital part for the non-specific response, were defined. They were drawn on the temporal mean image of the reconstructed activity distribution.

The TACs behavior for every individual pixel in those ROIs was examined and an average TAC was computed over each ROI and compared to the true TACs. In order to quantify the accuracy of the reconstructions, we compared for each ROI their relative deviation  $\mathcal{M}$  from the truth:

$$\mathcal{M} = \sqrt{\frac{\sum_{k \leq S} \sum_{i \in \text{ROI}} (x_{i, k}^{\text{true}} - x_{i, k})^2}{\sum_{k \leq S} \sum_{i \in \text{ROI}} x_{i, k}^{\text{true}2}} \quad (1)$$

Table I summarizes figures of merit for several reconstructions of the heart simulation comparing 2D and 3D versions of oSPECT and dEM, various regularizers, rotation protocols and temporal resolutions.

## VI. RESULTS AND DISCUSSION

In order to stabilize the reconstruction algorithm, we investigated ways to improve the condition number  $\text{cond}(H)$ . We observed that changing the problem  $(P)$  by tuning appropriately the weighting of the norm  $\|\cdot\|_w$  improved the reconstructions. For instance, the diagonal elements of  $R^T R$  show strong variations of several orders of magnitude. Prescaling by dividing each equation by its corresponding  $R^T R$  diagonal element improved the condition number  $\text{cond}(H)$  and stabilized the algorithm for some cases, but not for all. The improvement of the condition number is a study still under development. It is also expected that future versions of KNITRO will include the possibility of preconditioning the iterative solving of  $H(x) \cdot \Delta x = b$ . In parallel, the normalization of the objective function to rescale its values

close to 1 substantially improved the convergence and this feature was used in all the reconstructions presented in this paper.

### A. Myocardium

Among the regularizers we tested, the spatial Tychonoff and norm-1 asymmetric regularizers with a *roughness* parameter  $\alpha = 10^{-3}$  led to the best results. As seen in Table I, the asymmetric norm-1 regularizer provided the best result for the figure of merit  $\mathcal{M}$  in both myocardium and liver ROIs, and in the total image, but the Tychonoff regularizer generated a smoother image as seen in Fig. 4 and we therefore chose this latter for all reconstructions unless otherwise specified. We shall note that spatial regularization also provides a smoothing effect along the time dimension. The use of a temporal regularizer had a stronger smoothing effect on the TACs, and in particular removed significantly the peak artifact present in the liver TACs as we see in Fig. 3. However, the choice of this temporal regularizer has to be further investigated since the temporal Tychonoff regularizer we used in this study is very basic and led to excessively flattened TACs, in particular in the heard region.

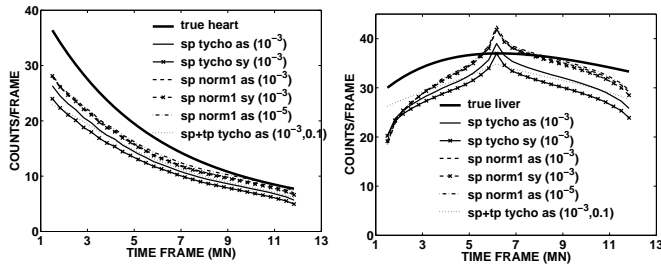


Fig. 3. Effect of choice of regularizers on reconstructed TACs for the heart (left) and the liver (right) regions.

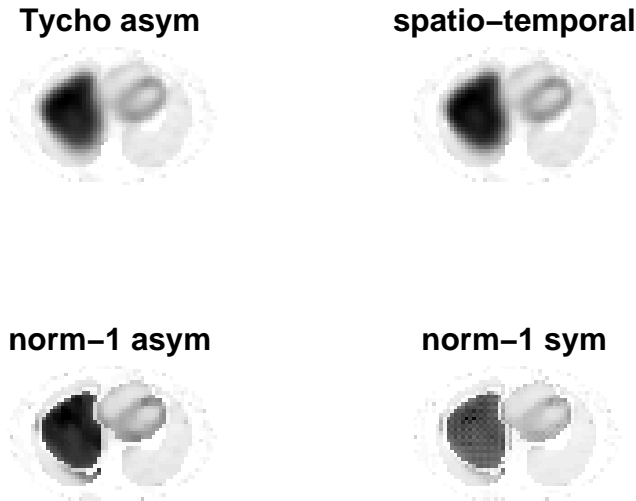


Fig. 4. Temporal mean of reconstructed transaxial slices with 4 different regularizers.

We investigated the accuracy of oSPECT reconstructions in 2D and 3D (+time) modes, and compared the results to the

TABLE I

SUMMARY OF THE FIGURES OF MERIT  $\mathcal{M}$  IN THE MYOCARDIUM AND LIVER REGIONS AND IN THE FULL RECONSTRUCTED IMAGE FOR THE SEVERAL RECONSTRUCTIONS PRESENTED (SEE TEXT).

Models	Myocardium	Liver	Total
2D oSPECT Tycho asym.	0.38	0.24	0.34
2D oSPECT norm-1 asym.	0.36	0.18	0.34
3D oSPECT	0.33	0.31	0.42
2D dEM	0.32	0.27	0.35
3D dEM	0.35	0.18	0.24
16 times - 1/2 rot	0.37	0.23	0.32
32 times - 1 rot	0.37	0.20	0.30
32 times - 2 rot	0.36	0.21	0.30
16 times - 2 rot	0.33	0.20	0.28
32 times - 3 rot	0.36	0.20	0.39
sp. Tycho asym. ( $10^{-3}$ )	0.38	0.24	0.34
sp. Tycho sym. ( $10^{-3}$ )	0.44	0.26	0.37
sp. norm-1 asym. ( $10^{-3}$ )	0.36	0.18	0.34
sp. norm-1 asym. ( $10^{-5}$ )	0.41	0.28	0.45
sp. norm-1 sym. ( $10^{-3}$ )	0.38	0.18	0.31
sp. Tycho asym. ( $10^{-3}$ )	0.40	0.21	0.32
+ tp. Tycho asym. (0.1)			

corresponding dEM reconstructions. All four reconstructions were initiated with the same static OSEM 3D reconstruction, and used the same temporal mask (prior information). Fig. 5 shows the individual and mean TACs for the heart and the liver regions. The monotonically decreasing mean TACs for the heart region showed no significant differences in the four reconstructions, and TACs agree well with the “truth”. When comparing the mean TACs for the liver region, dEM seems to perform slightly better than oSPECT which wrongly produces a peaked curve. However, investigating the TACs for individual pixels in liver, we see in Fig. 6 that the temporal behavior is more consistent with oSPECT than with dEM, this latter method reconstructing some individual TACs with a wrong temporal behavior. The improved consistency of the temporal behavior in a ROI with oSPECT is a significant feature since it may allow post-reconstruction segmentation based on the temporal characteristics as it is performed in [27]. When comparing the summarized figures of merit  $\mathcal{M}$  in Table I, we see that oSPECT 2D provides slightly better results than dEM 2D in the liver and in the total image. Indeed oSPECT reconstructs individual TACs with better consistency in ROIs exhibiting a uniform temporal pattern.

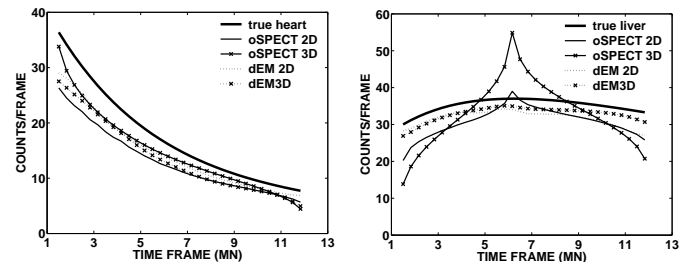


Fig. 5. Comparison of the mean TACs for the heart (left) and the liver (right) regions reconstructed with the 2D and 3D versions of oSPECT and dEM.

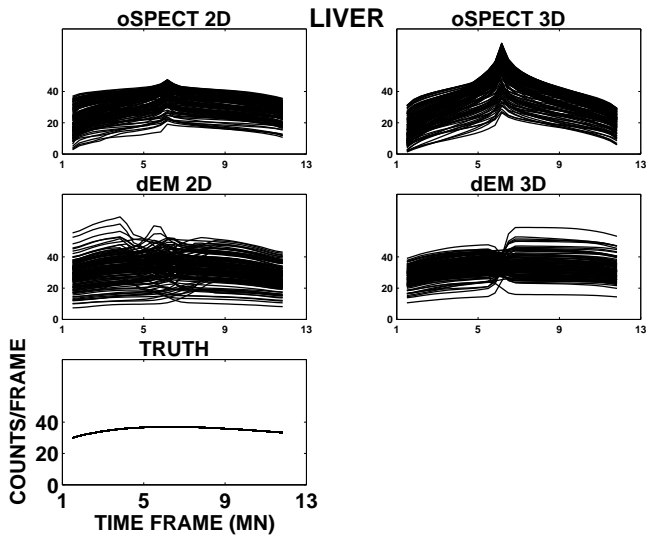


Fig. 6. TACs of individual voxels in liver reconstructed with the 2D and 3D versions of oSPECT and dEM.

This improvement also affects the image quality by reducing noise as can be seen on the temporal mean of a transaxial slice in Fig. 7. ROIs appear more homogeneous when reconstructed with oSPECT than with dEM. However, the 3D (+time) reconstruction with oSPECT is not yet satisfactory since its accuracy is decreased as compared with the 2D oSPECT reconstruction. Further work is planned to address this issue. Also, we expect to obtain additional improvement of the estimation of TACs by reducing their slope around the tentative peak positions, while adding a constraint  $c_p$  in  $(P)$  preserving the total number of counts, or by posteriori smoothing of the TACs. Also, we have seen in Fig. 3 that the elementary temporal regularizer we tested removed partly the peak artifact present in the liver TACs, and we expect further improvement with a more elaborate temporal regularizer.

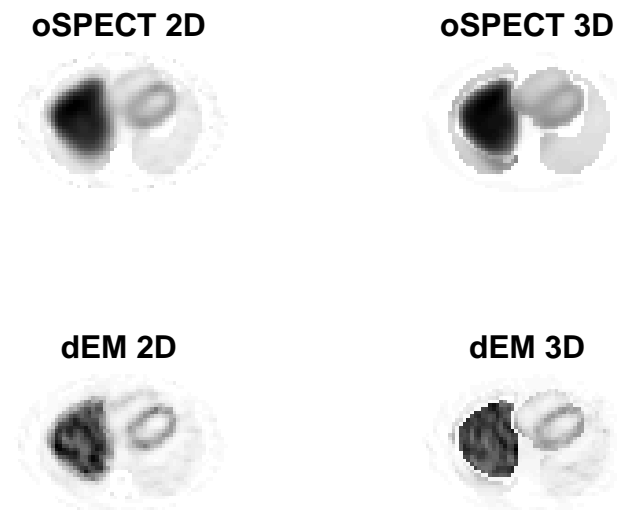


Fig. 7. Temporal mean of transaxial slices reconstructed with the 2D and 3D versions of oSPECT and dEM.

With the aim of improving reconstructions by reducing the dimension of the problem, we tried to reconstruct dynamic sinograms with a reduced number of time frames: the set of

projections acquired during two consecutive camera stops were reconstructed as a single time frame. Fig. 8 shows the resulting mean TACs for the heart and the liver regions and Fig. 9 the corresponding transaxial slices of the temporal means. This approach improved the reconstructions as seen in Table I. Although the improvement is moderate, this approach may be of great value since it reduces significantly the reconstruction cpu time, this latter being roughly proportional to the number of reconstructed time frames. Reducing temporal resolution may also be necessary in reconstructing multiple rotations scans with a large number of rotation as the number of time frames in this case may be too large to be computationally feasible.

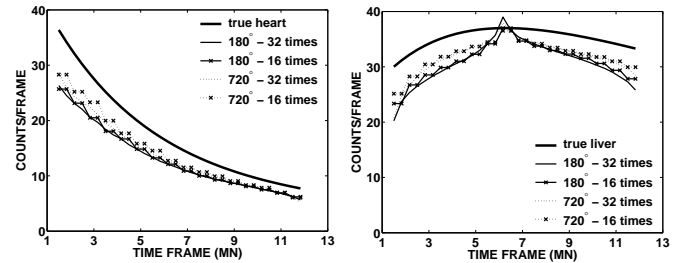


Fig. 8. Effect of the temporal resolution on reconstructed TACs for the heart (left) and the liver (right) regions.

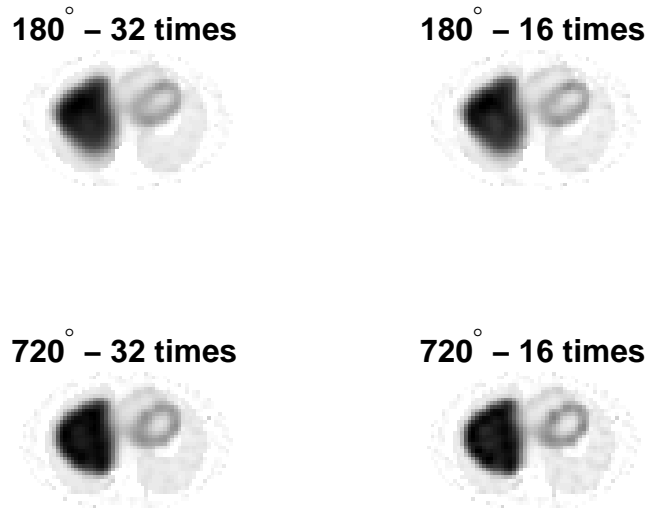


Fig. 9. Temporal mean of transaxial slices of the standard cardiac protocol and two rotations protocol studies reconstructed with full temporal resolution (32 time frames) and with 16 time frames.

It seemed likely that a multiple rotations protocol would lead to a better reconstruction (as long as the temporal resolution is also reduced to avoid the increase of the number of unknowns in the problem) since in this case the number of projection data is larger than in a single rotation scan. However, in the case where the number of projection data remained the same, we studied the influence of the number of rotations on reconstruction quality. Thus, we compared image reconstructions of three acquisition protocols using one, two and three full rotations. The standard cardiac scan over 180° was used as reference. As can be seen in Fig. 10 presenting the

reconstructed mean TACs for the heart and the liver regions, as well as in Table I, a full rotation is to be favoured over a  $180^\circ$  rotation. Image quality of the reconstructed transaxial slices is also improved as shown in Fig. 11. In particular, heart and liver spatial activities distributions are more uniform and closer to the true distributions in the full rotation study than in the half rotation study. However, this result is also due in part to the larger number of projections in the full rotation protocol.

When comparing one, two or three full rotations (with the same number of projections), there was no significant difference in reconstruction quality. Those results suggest that the greater the number of projection data and the less under-determined the system is, the better will be the reconstruction. But the projection sampling can be indifferently chosen over a single or multiple rotations.

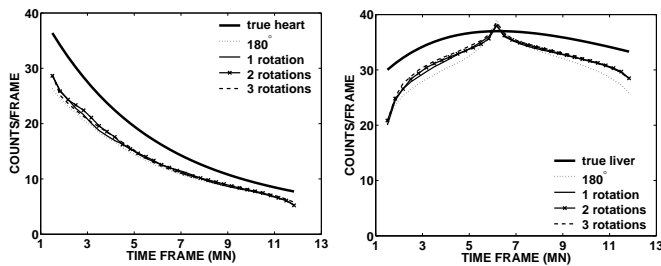


Fig. 10. Effect of multiple rotations on reconstructed TACs for the heart (left) and the liver (right) regions.

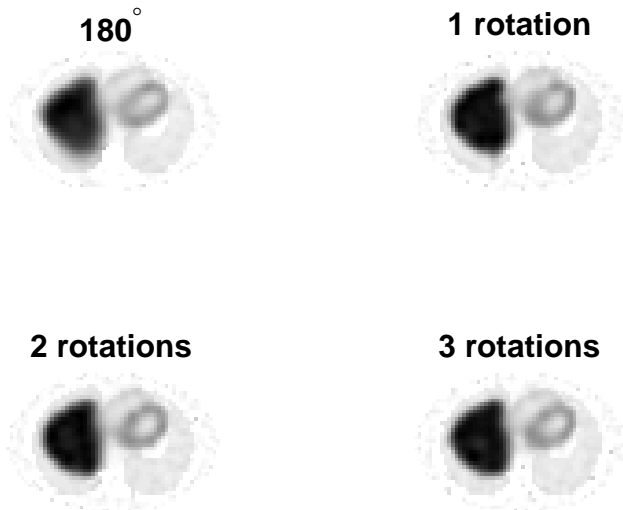


Fig. 11. Temporal mean of reconstructed transaxial slices of the standard cardiac protocol, one, two and three rotations protocol studies.

### B. Brain

The brain simulation was reconstructed using oSPECT 2D and 3D. Our preliminary results showed a reasonably good agreement between the true and the reconstructed mean TACs for the putamens, caudate nuclei and occipital regions as shown in Fig. 12 and reconstructed transaxial slices resemble the true one as we see in Fig. 13. As in the heart simulation, the

activity distribution reconstructed with oSPECT 2D was closer to the “truth” than the activity reconstructed with oSPECT 3D. However, oSPECT performed more efficiently in this cerebral study than in the myocardial study since the number of dynamic voxels, and hence variables was significantly smaller in the brain. Those results show that oSPECT has the potential to be clinically valuable for dynamic brain studies.

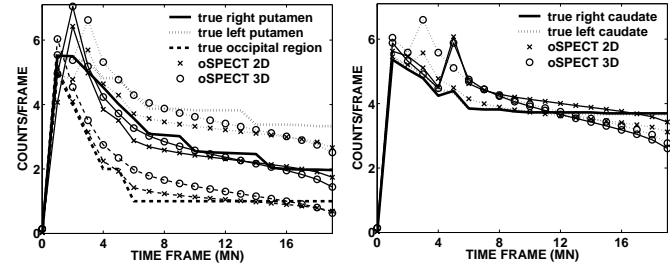


Fig. 12. TACs of the true brain phantom and 2D/3D oSPECT reconstructions in putamens, caudate nuclei and occipital region.



Fig. 13. Temporal mean of a transaxial slice of the brain simulation reconstructed with oSPECT 2D and 3D.

## VII. CONCLUSION

This paper presents oSPECT, a new approach to reconstruct spatio-temporal activity distributions from dynamic SPECT projection data acquired with a single or multiple slow rotations. It is based on a large-scale nonlinear constrained optimization method that takes curvature information into account to speed up convergence.

We tested the performance of oSPECT using data from a dynamic anthropomorphic phantom that simulates myocardial perfusion of  $^{99m}\text{Tc}$ -Teboroxime, as well as on a simulated brain study with  $^{123}\text{I}$ -FP-CIT, a dynamic presynaptic marker for SPECT of the dopaminergic neurotransmission system.

Our first results show a reasonably good agreement between the true and the reconstructed activity distributions. We show that oSPECT performs slightly better than dEM in the 2D case and that individual TACs behave more consistently in dynamically homogeneous regions. This feature is essential for “post-reconstruction” temporal segmentation.

Our results also suggest that the greater the number of projection data and the less under-determined the system is, the better will be the reconstruction. But the projection sampling can be indifferently chosen over a single or multiple rotations.

Although oSPECT and the elementary regularizers presented in this paper did not provide much better dynamic reconstructions than previous methods, it is a very flexible and versatile tool that can be adapted to various physiological problems and has a great potential of improvements through the use of appropriate constraints and regularizing terms.

Future work will include:

- i) the investigation of suitable spatial and temporal regularizers and constraints to improve accuracy of reconstructions,
- ii) the development of a weighting procedure to speed up convergence in chosen regions of interest,
- iii) the development of a method based on the fit of "hat functions" to determine the dynamic *a priori* information needed by oSPECT.

#### ACKNOWLEDGMENT

The authors would like to thank T. Farncombe for providing the 3D version of the dEM algorithm.

#### REFERENCES

- [1] B. Mazoyer, R. Huesman, T. Budinger, and B. Knittel, "Dynamic PET data analysis," *J. Computer Assisted Tomography*, vol. 10, pp. 645–653, 1986.
- [2] Y. Choi, S.-C. Huang, R. Hawkins, W. Kuhle, M. Dahlbom, C. Hoh, J. Czernin, M. Phelps, and H. Schelbert, "A simplified method for quantification of myocardial blood flow using nitrogen-13-ammonia and dynamic pet," *J. Nucl. Med.*, vol. 34, pp. 488–497, 1993.
- [3] W. Cai, D. Feng, and R. Fulton, "Content-based retrieval of dynamic pet functional images," *IEEE Trans. Information Technology in Biomedicine*, vol. 4, no. 2, pp. 227–234, 2000.
- [4] T. Nichols, J. Qi, E. Asma, and R. Leahy, "Spatiotemporal reconstruction of list-mode pet data," *IEEE Trans. Med. Imag.*, vol. 21, no. 4, pp. 396–404, 2002.
- [5] H. Iida and S. Eberl, "Quantitative assessment of regional myocardial blood flow with thallium-201 and SPECT," *J. Nucl. Cardiology*, vol. 5, pp. 313–331, 1998.
- [6] I. Odana, M. Ohkubo, and T. Yokoi, "Noninvasive quantification of cerebral blood flow using  $^{99m}\text{Tc}$ -ECD and SPECT," *J. Nucl. Med.*, vol. 40, pp. 1737–1744, 1999.
- [7] K. Nakajima, J. Taki, H. Bunko, M. Matsudaira, A. Muramori, I. Matsunari, K. Hisada, and T. Ichihara, "Dynamic acquisition with a three-headed SPECT system: application to technetium  $^{99m}\text{Tc}$ -SQ30217 myocardial imaging," *J. Nucl. Med.*, vol. 32, pp. 1273–1277, 1991.
- [8] K. Kitagawa, K. Takeda, K. Saito, S. Okamoto, K. Makino, H. Maeda, and T. Ichihara, "Differences in fatty acid metabolic disorder between ischemic myocardium and doxorubicin-induced myocardial damage: assessment using BMIPP dynamic SPECT with analysis by the rutland method," *J. Nucl. Med.*, vol. 43, pp. 1286–1294, 2002.
- [9] M. Limber, A. Celler, J. Barney, M. Limber, and J. Borwein, "Direct reconstruction of functional parameters for dynamic SPECT," *IEEE Trans. Nuc. Sci.*, vol. 42, pp. 1249–1256, 1995.
- [10] R. Huesman, B. Reutter, G. Zeng, and G. Gullberg, "Kinetic parameter estimation from SPECT cone-beam projection measurements," *Phys. Med. Biol.*, vol. 43, no. 4, pp. 973–982, 1998.
- [11] B. Reutter, G. Gullberg, and R. Huesman, "Kinetic parameter estimation from attenuated SPECT projection measurements," *IEEE Trans. Nuc. Sci.*, vol. 45, no. 6, pp. 3007–3013, 1998.
- [12] A. Sitek, E. D. Bella, and G. Gullberg, "Factor analysis of dynamic structures in dynamic SPECT imaging using maximum entropy," *IEEE Trans. Nuc. Sci.*, vol. 46, no. 6, pp. 2227–2232, 1999.
- [13] D. Kadmas and G. Gullberg, "4D maximum *a posteriori* reconstruction on dynamic SPECT using a compartmental model-based prior," *Phys. Med. Biol.*, vol. 46, pp. 1553–1574, 2001.
- [14] D. Kadmas, E. DiBella, R. Huesman, and G. Gullberg, "Analytical propagation of errors in dynamic SPECT: estimators, degrading factors, bias and noise," *Phys. Med. Biol.*, vol. 44, no. 8, pp. 1997–2014, 1999.
- [15] J. Maeght, D. Noll, and S. Boyd, "Dynamic emission tomography - regularization and inversion," in *Canadian Math. Society, Conf. Proc.*, 1999.
- [16] T. Farncombe, A. Celler, D. Noll, J. Maeght, and R. Harrop, "Dynamic SPECT imaging using a single camera rotation (dSPECT)," *IEEE Trans. Nuc. Sci.*, vol. 46, no. 4, pp. 1055–1061, 1999.
- [17] H. Bauschke, D. Noll, A. Celler, and J. Borwein, "An EM algorithm for dynamic SPECT tomography," *IEEE Trans. Med. Imag.*, vol. 18, no. 3, pp. 252–261, 1999.
- [18] T. Farncombe, A. Celler, D. Noll, J. Maeght, and R. Harrop, "The incorporation of organ uptake into dynamic SPECT (dSPECT) image reconstruction," *IEEE Trans. Nuc. Sci.*, vol. 48, no. 1, pp. 3–9, 2001.
- [19] T. Farncombe, M. King, A. Celler, and S. Blinder, "A fully 4d expectation maximization algorithm using gaussian diffusion based detector response for slow camera rotation dynamic SPECT," in *Proceedings of the 2001 International Meeting on Fully 3D Image Reconstruction in Radiology and Nuclear Medicine*, October 2001.
- [20] A. Celler, S. Blinder, D. Noll, T. Tyler, F. Duclercq, and R. Harrop, "Investigation of the dynamic SPECT (dSPECT) method for teboroxime using a 4-d kinetic thorax model dMCAT," in *Proceedings of the 2001 International Meeting on Fully 3D Image Reconstruction in Radiology and Nuclear Medicine*, October 2001.
- [21] Z. Liang, J. Cheng, and J. Ye, "Validation of the central-ray approximation for attenuated depth-dependent convolution in quantitative SPECT reconstruction," *Phys. Med. Biol.*, vol. 42, no. 2, pp. 433–439, 1997.
- [22] S. Blinder, A. Celler, W. G. D. Thomson, and R. Harrop, "Experimental verification of 3D detector response compensation using the OSEM reconstruction method," in *2001 IEEE Nuclear Science Symposium and Medical Imaging Conference Record*, November 2001, pp. M13C–11.
- [23] C. Blondel, D. Noll, J. Maeght, and T. Farncombe, "Comparison of different figure of merit functions for dynamic single photon emission computed tomography (dSPECT)," in *2000 IEEE Nuclear Science Symposium Conference Record*, November 2000, pp. 15.151–15.155.
- [24] R. Waltz and J. Nocedal, "Knitro user's manual," Northwestern University, Evanston, Illinois, Technical Report OTC-2003/5, 2003.
- [25] J. Logan, J. Fowler, N. Volkow, G. Wang, Y. Ding, and D. Alexoff, "Distribution volume ratios without blood sampling from graphical analysis of pet data," *J. Cereb. Blood Flow Metabol.*, vol. 16, pp. 834–840, 1996.
- [26] M. Ichise, J. H. Meyer, and Y. Yonekura, "An introduction to PET and SPECT neuroreceptor quantification models," *J. Nucl. Med.*, vol. 42, pp. 755–763, 2001.
- [27] K. D. Toennies, A. Celler, S. Blinder, T. Moeller, and R. Harrop, "Scatter segmentation in dynamic SPECT images using principal component analysis," in *SPIE Medical Imaging 2003, San Diego, CA*, February 2003.